Probing the Contribution of Lateral Pathways to Out-of-Plane Charge Transport in Organic Bulk Heterojunctions

*Pravini S. Fernando, Jeremy S. Mehta, Detlef-M. Smilgies, and Jeffrey M. Mativetsky**

P. S. Fernando, Dr. J. S. Mehta, Prof. J. M. Mativetsky

Department of Physics, Applied Physics and Astronomy, Binghamton University, Binghamton, New York, 13902, United States
E-mail: jmativet@binghamton.edu

Dr. D.-M. Smilgies, Prof. J. M. Mativetsky

Materials Science and Engineering Program, Binghamton University, Binghamton, New York, 13902, United States

Keywords: organic solar cells, bulk heterojunctions, charge transport

The nanoscale interpenetrating electron donor-acceptor network in organic bulk heterojunction (BHJ) solar cells results in efficient charge photogeneration but creates complex three-dimensional pathways for charge transport. At present, little is known about the extent to which out-of-plane charge flow relies on lateral electrical connectivity. In this work, we introduce a procedure, based on conductive atomic force microscopy, to quantify lateral current spreading during out-of-plane charge transport. Using the developed approach, we study the dependence of lateral spreading on BHJ phase separation, composition, and molecule type (small molecule versus polymer). In the small molecule BHJ, *p*-DTS(FBTTh$_2$)$_2$:PC$_{71}$BM, we observe an increase in lateral hole current spreading as the population of donor crystallites, bearing an edge-on molecular orientation, is increased. When integrated into BHJs, the polymer donor P3HT leads to greater lateral hole current spreading and more spatially uniform charge transport than the small molecule donor, owing to in-plane charge transport along the polymer

backbone. Through the newly introduced electrical characterization scheme, these experiments bring to light the role of lateral electrical connectivity in assisting charge navigation across BHJs.

1. Introduction

Solution processed bulk heterojunction (BHJ) organic solar cells (OSCs) provide a route towards lightweight, flexible, and optically tunable photovoltaics[1–5] with power conversion efficiencies (PCE) that currently exceed 26%[6–9] and 18%[10–13] for indoor and outdoor conditions, respectively. Although the BHJ's nanoscale interpenetrating electron donor-acceptor network can efficiently photogenerate charge, it also creates tortuous pathways for charge collection. Efficient out-of-plane charge transport plays a crucial role in OSC performance and is highly sensitive to the BHJ morphology that can include pure and finely mixed donor and acceptor domains, crystalline and amorphous regions, varying molecular orientations, and vertical phase separation.[14,15] These structural features lead to three-dimensional charge percolation networks that involve both vertical and lateral transport pathways for electrons to travel through the electron accepting material and for holes to flow through the electron donating material.[16–20] Unlike the case of single component films, BHJs necessitate lateral pathways for electrons (holes) to bypass donor (acceptor) regions.

Efforts to enhance out-of-plane charge transport in BHJs have emphasized the need for promoting vertical transport channels, though little consideration has been given to the role of lateral pathways in assisting vertical charge flow. Notably, several studies have reported improved hole mobilities and PCEs in BHJs with mixed face-on and edge-on donor stacking when compared to BHJs featuring a

highly face-on donor phase.[21–25] Even though face-on stacking should promote out-of-plane transport,[26–29] these studies suggest that some degree of lateral transport, favored by edge-on molecular stacking, enables efficient out-of-plane charge transport in BHJs. In support of this conclusion, a recent study from our group noted that the out-of-plane hole mobility in a small molecule BHJ is strongly correlated with the population of in-plane π-π stacking that promotes lateral transport.[20] Percolation analysis of BHJs with varying donor fractions has also led to the conclusion that charge transport in BHJs is fundamentally three-dimensional, involving vertical and lateral channels.[19,20]

Nevertheless, the degree to which lateral current spreading contributes to out-of-plane charge transport in BHJs is currently unknown, as there are no experimental methods to directly study this property. Percolation analysis, which involves analyzing charge transport in a series of samples of varying composition, is only applicable for compositions near the percolation threshold and does not provide a measure of the in-plane current spreading.[19,20,30] The integration of BHJ active layers into organic field-effect transistors (OFETs) enables in-plane charge carrier mobility measurements.[19,31] The measurement geometry, however, differs from the vertically stacked structure of OSCs, while the application of a gate voltage during OFET operation induces an increased charge carrier density within a thin two-dimensional layer of the active material. Additionally, the use of a dielectric beneath the OFET active layer changes the substrate surface energy relative to the OSC case and can impact active layer growth,[32,33] creating further differences between the charge transport measured in OFETs and OSCs. Transmission electron tomography can provide insight into the network structure of the active layer,[16,17] but does not probe electrical connectivity. The lack of tools to measure the contribution of lateral pathways to out-of-plane charge transport in BHJs limits present

understanding of the electrical connectivity requirements for optimal charge transport in organic BHJs.

In this study, we introduce a means of quantifying lateral current spreading during out-of-plane charge transport using conductive atomic force microscopy (C-AFM). With this approach, we elucidate the effects of donor-acceptor phase separation, active layer composition, and molecule type on lateral current spreading within BHJs. These experiments bolster the case that in-plane π-π stacking promotes three-dimensional electrical connectivity and indicate that polymer-based BHJs benefit from charge transport along the polymer backbone.

2. Results

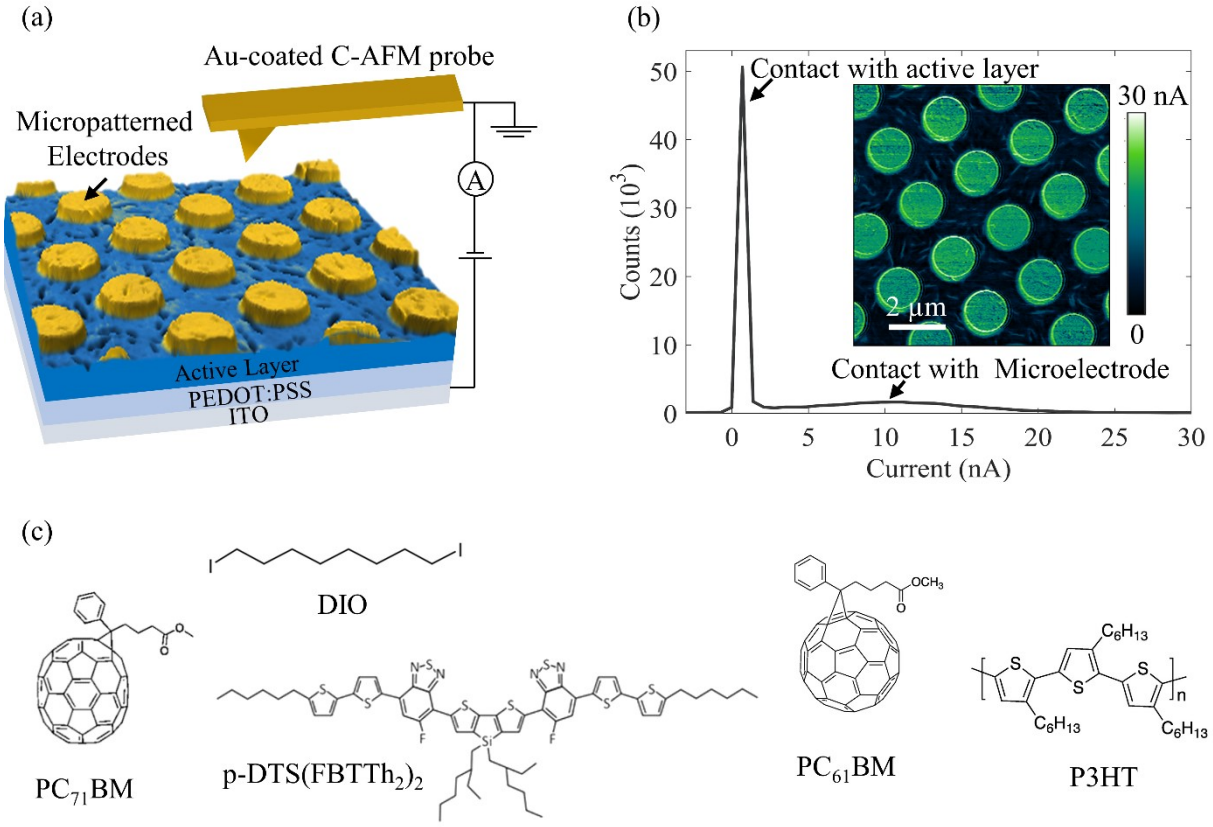

Figure 1. (a) Setup for determining the current spreading area during C-AFM measurements. The sample consists of microelectrodes patterned on an active layer coated on PEDOT:PSS/ITO. (b) A representative current map and the corresponding histogram for a *p*-DTS(FBTTh$_2$)$_2$ film. (c) Molecular structure of *p*-DTS(FBTTh$_2$)$_2$, P3HT, $PC_{71}BM$, $PC_{61}BM$, and the additive DIO.

Figure 1a depicts the C-AFM setup for quantifying lateral current spreading during out-of-plane charge transport through an organic active layer. The procedure uses an array of micropatterned Au electrodes of known area deposited onto the active layer, while indium tin oxide (ITO) coated with poly(3,4-ethylenedioxythiophene) polystyrene sulfonate (PEDOT:PSS) serves as a bottom electrode. C-AFM current maps, in which the C-AFM probe serves as a movable nanoscale top electrode, are

recorded over a sample region that includes both the micropatterned electrodes and the bare film. When the probe is in direct contact with the active layer, lateral current spreading takes place due to the diverging electric field between the sharp nanoscale C-AFM probe and the planar bottom electrode.[34,35] The current spreading also depends on the film structure, which can introduce charge transport anisotropy.[36–38] In contrast, when the probe is in contact with a microelectrode, the electric field drops sharply at the microelectrode edge, with little spread relative to microelectrode size.[35] The C-AFM current recorded from the known current collecting area of the microelectrode serves as a calibration standard. A similar measurement approach has been employed by our group to estimate the effective charge collection area during C-AFM, making it possible to obtain calibrated conductivity and current density maps.[35] In this study, we propose using the effective current spreading radius as a measure of lateral transport pathway availability in organic active layers.

Figure 1b presents an example of a current map for an active layer comprised of the small molecule electron donor, 7,7′-(4,4-bis(2-ethylhexyl)-4*H*-silolo[3,2-b:4,5-*b*′]dithiophene-2,6-diyl)bis(6-fluoro-4-(5′-hexyl-[2,2′-bithiophen]-5-yl)benzo[*c*]- [1,2,5]thiadiazole) (*p*-DTS(FBTTh$_2$)$_2$), along with the corresponding current histogram. The structure of the molecules under study are shown in Figure 1c. The current map (Figure 1b) shows circular high current regions where the C-AFM probe is in contact with the Au microelectrodes and current is collected over the entire area of a microelectrode. A much lower current is recorded when the sharp C-AFM probe is in direct contact with the active layer. In the corresponding current histogram, the sharp peak at 0.17 nA represents the current when the probe is in direct contact with the active layer and the broad peak centered at 9.2 nA represents the current when the probe is in contact with the micropatterned electrodes.

Since the current-carrying area below the microelectrode is approximately equal to the microelectrode area,[35] the average current density (J) can be calculated by dividing the average current through a microelectrode (I_m) by the area of the microelectrode (A_m):

$$J = I_m/A_m \quad (1)$$

If J is approximated to be constant throughout the film, the effective current spreading area (A_{eff}) beneath the C-AFM probe can be obtained from:

$$A_{eff} = I_p/J, \quad (2)$$

where I_p is the average current measured when the C-AFM probe is in contact with the active layer. A_{eff} depends on the lateral current spreading caused by factors such as the molecular structure, molecular orientation, and film morphology. A_{eff} also depends on the active layer thickness and applied bias voltage.[35] Therefore, when used as a tool to measure lateral spreading, the bias voltage and film thickness must be kept constant.

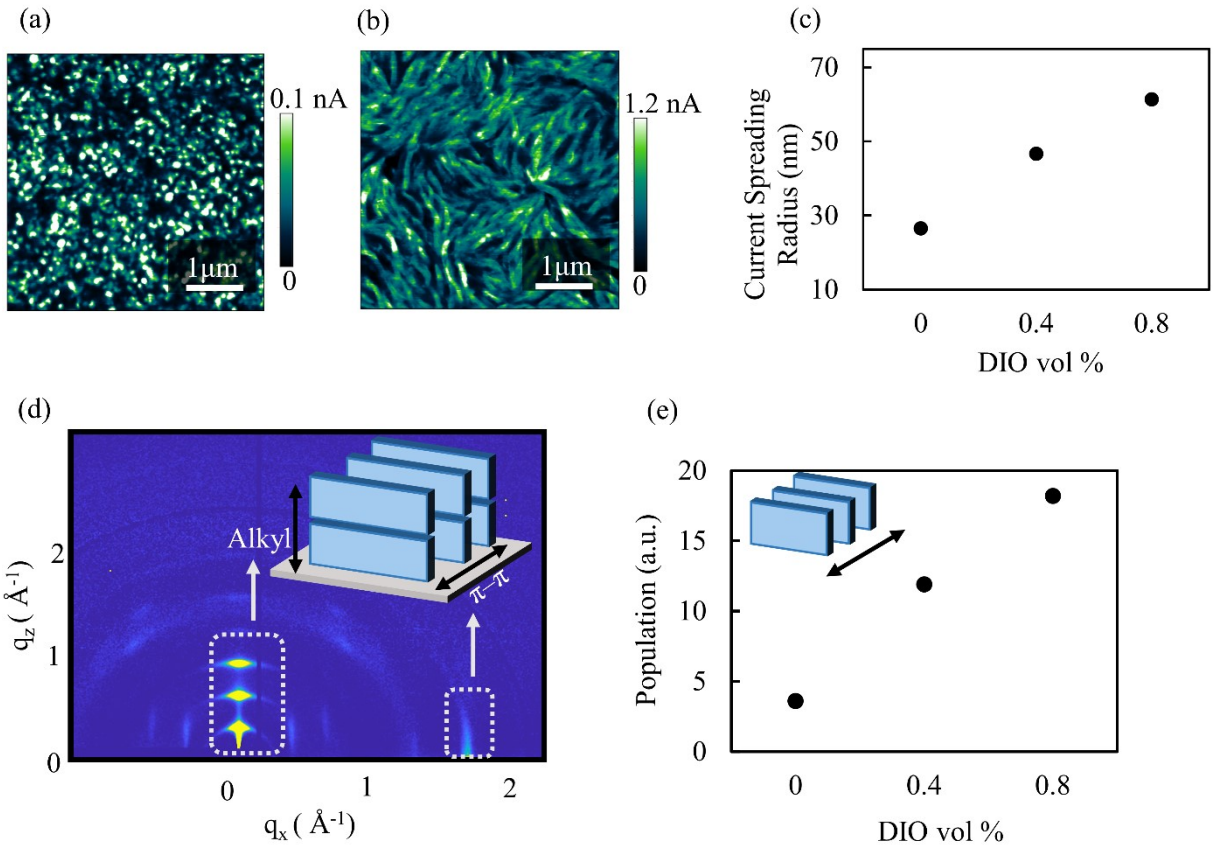

Figure 2. C-AFM current maps for *p*-DTS(FBTTh$_2$)$_2$: PC$_{71}$BM BHJ films with a donor weight fraction φ_{DTS} = 0.6 and a DIO volume concentration of (a) 0% and (b) 0.8%. (c) Variation of current spreading radius with DIO vol. %. (d) GIWAXS pattern for φ_{DTS} = 0.6, 0.4 vol. % DIO, with a schematic showing out-of-plane alkyl stacking and in-plane π−π stacking of *p*-DTS(FBTTh$_2$)$_2$. (e) Dependence of in-plane π−π stacking population on DIO vol. %.

For insight into the effect of donor-acceptor phase separation on lateral current spreading, a series of *p*-DTS(FBTTh$_2$)$_2$:PC$_{71}$BM BHJ active layers were prepared with a constant donor weight fraction

(φ_{DTS}) of 0.6 and varying amounts of solvent additive 1,8-diiodooctane (DIO). DIO is widely used in *p*-DTS(FBTTh$_2$)$_2$:PC$_{71}$BM films to promote phase separation and crystallization by slowing the solvent evaporation rate.[26,39,40] The highest reported performance for *p*-DTS(FBTTh$_2$)$_2$:PC$_{71}$BM solar cells, an 8.94% power conversion efficiency, was achieved with φ_{DTS} = 0.6 and 0.4 vol. % DIO.[41]

C-AFM current images for *p*-DTS(FBTTh$_2$)$_2$:PC$_{71}$BM BHJ films with 0 and 0.8 vol. % DIO (φ_{DTS} = 0.6) are shown in **Figures 2**a and 2b. The high work function of the Au-coated C-AFM probe and the PEDOT:PSS hole transport layer allows hole-only charge transport by blocking the injection of electrons. Therefore, in the current images, bright regions correspond to high hole current in well-connected donor domains.[42] The hole current shows a strong dependence on the degree of phase separation. At 0 vol. % DIO (Figure 2a), the average hole current is 51.6 pA and small conductive spots can be seen, which span from tens to hundreds of nanometers in size. At 0.8% DIO, the average hole current increases to 397 pA and we observe conductive, laterally connected fibers with lengths greater than 1 µm.

Increased phase separation is linked not only to improved out-of-plane hole transport, but it also increases lateral current spreading, as shown in Figure 2c. The effective current spreading radius for a film with no DIO additive was 27 nm, approximately three times the mechanical contact radius between the probe and sample, according to the Johnson-Kendall-Roberts (JKR) and Derjaguin-Muller-Toporov (DMT) contact models.[34,43] The effective current spreading radius for 0.4 and 0.8 vol. % DIO was 47 nm and 61 nm, respectively, demonstrating increased lateral electrical connectivity in these films with larger fibrillar *p*-DTS(FBTTh$_2$)$_2$ domains.

The observed current spreading can be attributed in part to the predominantly edge-on molecular orientation of the donor molecules. A grazing incidence wide angle X-ray scattering (GIWAXS) pattern for a *p*-DTS(FBTTh$_2$)$_2$:PC$_{71}$BM film (φ_{DTS} = 0.6, 0.4 vol. % DIO) is shown in Figure 2d. A distinct (001) alkyl stacking peak at q_z = 0.25 Å^{-1}, along with higher order (002) and (003) reflections, as well as a prominent (141) in-plane π−π stacking peak at q_x = 0.75 Å^{-1} are evidence of edge-on stacked *p*-DTS(FBTTh$_2$)$_2$.[20,44,45] An edge-on orientation, with π−π stacking parallel to the substrate, favors in-plane transport.[46,47] The *p*-DTS(FBTTh$_2$)$_2$:PC$_{71}$BM BHJs with varying degrees of phase separation (φ_{DTS} = 0.6, DIO vol. % = 0, 0.4 and 0.8) all exhibited a predominantly edge-on orientation (see Supporting Information, Figure S6). The crystallite population associated with in-plane π−π stacking is shown in Figure 2e. The in-plane π−π crystallite population was quantified by integrating the area under the (141) peak over an angular width of 20°.[20,48] The rise in the in-plane π−π population with increasing DIO amount is consistent with the observed concurrent increase in the lateral hole current spreading radius.

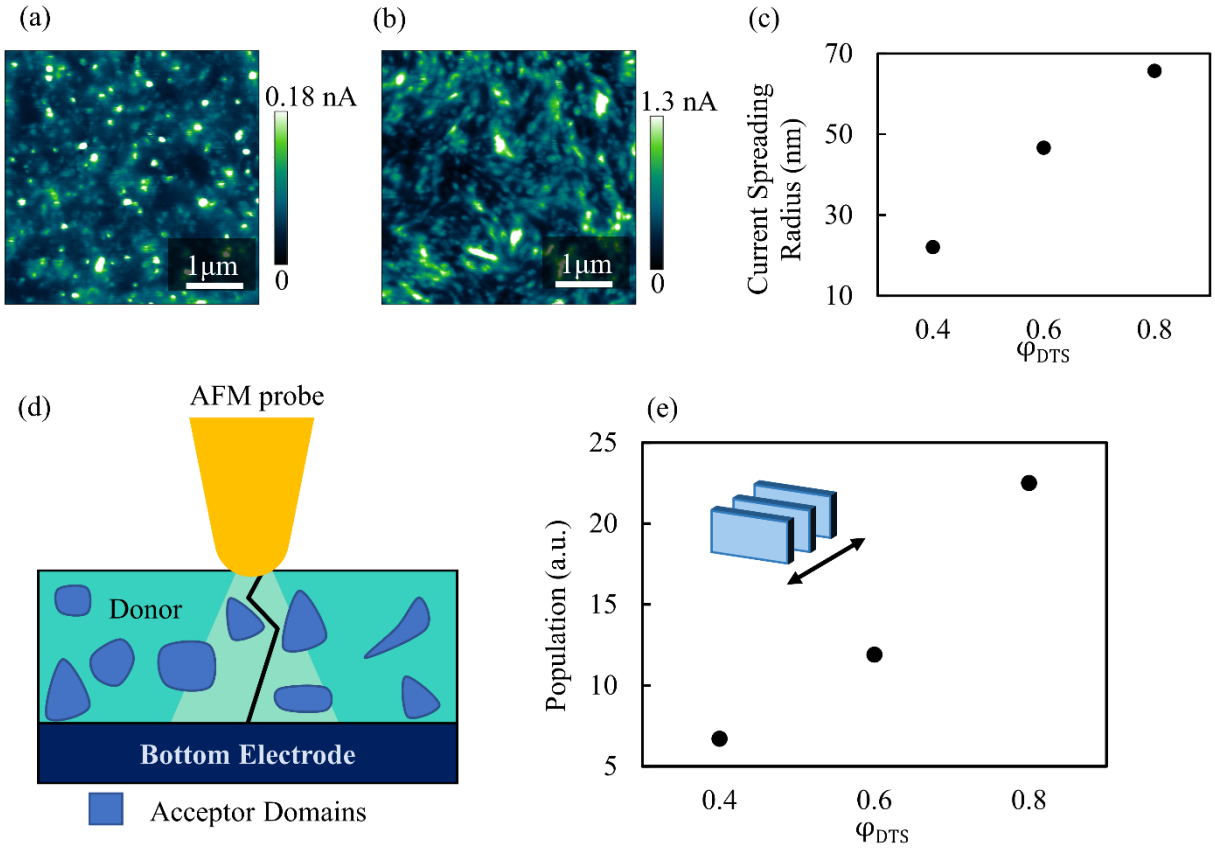

Figure 3. C-AFM current maps for *p*-DTS(FBTTh$_2$)$_2$:PC$_{71}$BM BHJ active layer with 0.4 vol. % DIO and a *p*-DTS(FBTTh$_2$)$_2$ weight fraction (φ_{DTS}) of (a) 0.4, and (b) 0.8. (c) Variation of current spreading radius with φ_{DTS}. (d) Schematic showing hole current spreading hindered by acceptor domains (e) Dependence of in-plane π–π stacking population on φ_{DTS}.

To investigate the effect of active layer composition on lateral current spreading, we varied φ_{DTS} from 0.4 to 0.8, while maintaining a constant DIO amount of 0.4 vol. %. At φ_{DTS} = 0.4, the hole current map (**Figure 3**a) features isolated conductive spots that are tens of nanometers in size. For higher φ_{DTS} (Figure 3b and Supporting Information, Figure S1), elongated fibrillar structures can be seen, which extend up to hundreds of nanometers in length at φ_{DTS} = 0.8 (Figure 3b). Concurrently,

the average hole current increases from 23 pA (φ_{DTS}= 0.4) to 320 pA (φ_{DTS}= 0.8) and the lateral current spreading radius increases from 22 nm to 66 nm over the investigated film composition range.

The crystal structure of the films play a key role in the lateral current spreading as the film composition is varied. GIWAXS (shown in Supporting Information Figure S7) reveals a predominantly edge-on *p*-DTS(FBTTh$_2$)$_2$ orientation for each of the examined active layer compositions. As shown in Figure 3e, the in-plane π−π population increases with φ_{DTS}, contributing to the rise in lateral hole current spreading as the donor content is increased. The current spreading range while varying DIO % (Figure 2c) and φ_{DTS} (Figure 3c) are similar, which we attribute to the comparable π−π crystallite populations that are present across the two data sets (Figure 2e, Figure 3e). The increase in hole current and lateral spreading with φ_{DTS} can also be attributed in part to the reduced disruption of hole current by the acceptor phase, since acceptor domains act as barriers for hole transport, as illustrated in Figure 3d. In support of this conclusion, the smallest observed current spreading radius among the above data sets occurs when ϕ_{DTS} = 0.4, owing to the large fraction of PC$_{71}$BM disrupting hole flow, while the largest observed current spreading radius occurs when ϕ_{DTS} = 0.8, owing to the small fraction of PC$_{71}$BM disrupting hole flow.

Notably, when comparing *p*-DTS(FBTTh$_2$)$_2$:PC$_{71}$BM BHJs with single component *p*-DTS(FBTTh$_2$)$_2$ films, a drastically higher in-plane π−π population is observed in the single component case (**Table 1**). This upsurge in π−π population in pure *p*-DTS(FBTTh$_2$)$_2$ films can be explained by an absence of acceptor domains that disrupt donor crystallite growth. Correspondingly, the current spreading radius also

shows a sharp increase, from 27 nm in φ_{DTS} = 0.6, 0% DIO BHJ films to 120 nm in pure *p*-DTS($FBTTh_2$)$_2$.

A drastic increase in lateral hole current spreading was similarly observed when comparing polymer-based BHJs and single component polymer donor films. As shown in Table 1, BHJ films comprised of the polymer donor poly(3-hexylthiophene-2,5-diyl) (P3HT) and the fullerene acceptor (6,6)-Phenyl C_{61} butyric acid methyl ester ($PC_{61}BM$) exhibited a current spreading radius of 75 nm, while single component P3HT films had a significantly greater current spreading radius of 190 nm. Interestingly, we observe much higher lateral current spreading for the polymer-based BHJ and single component films, when compared to the corresponding small molecule films.

Table 1. Current spreading radius and mean hole mobility for BHJ (φ = 0.6, 0% DIO) and single component donor films.

Sample	Current Spreading Radius [nm]	Hole Mobility [cm^2/ V.s]	In-plane π–π stacking population [a.u.]
p-DTS($FBTTh_2$)$_2$:$PC_{71}BM$	27	1.4×10^{-4}	4
p-DTS($FBTTh_2$)$_2$	120	2.9×10^{-4}	176
P3HT:$PC_{61}BM$	75	1.5×10^{-4}	3

P3HT	190	1.9×10^{-4}	6

GIWAXS shows that the P3HT in BHJ and single component films are predominantly edge-on with respect to the substrate (see the Supporting Information, Figure S9). Much like the small molecule films, the pure polymer films exhibit an increased in-plane π–π population relative to the BHJ; however, the in-plane π–π population for the pure polymer films is far lower than that for the pure small molecule films. We therefore, attribute the observed high lateral spreading in the polymer films to efficient charge transport along the polymer backbone,[49,50] rather than a high population of in-plane π–π stacking. For very thin (25 nm), highly crystalline P3HT films with predominantly edge-on molecular stacking, we measure a current spreading radius of 144 nm, showing a remarkable combined effect of charge transport along the polymer backbone and in-plane π–π stacking on lateral electrical connectivity (Supporting Information Figure S10).

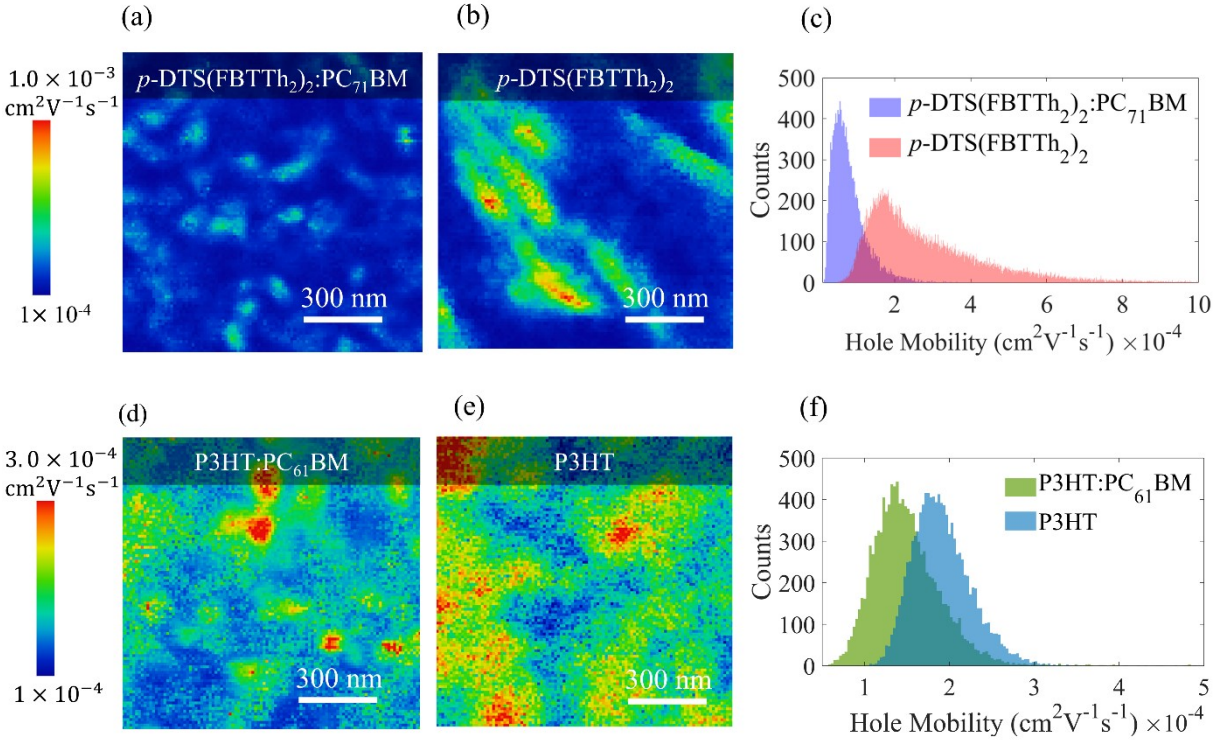

Figure 4. Hole mobility maps for (a) *p*-DTS(FBTTh$_2$)$_2$:PC$_{71}$BM and (b) *p*-DTS(FBTTh$_2$)$_2$ with 0 vol. % DIO, along with (c) the corresponding hole mobility histogram. Hole mobility maps for (d) P3HT:PC$_{61}$BM and (e) P3HT, along with (f) the corresponding hole mobility histogram.

To learn more about the interplay between lateral current spreading and electrical connectivity in polymer and small molecule systems, we performed hole mobility mapping measurements using a recently developed C-AFM mode, point-by-point current-voltage (PPIV) mapping.[20,42,43] In PPIV mapping, large arrays of current-voltage curves are analyzed to extract local quantitative metrics. Here, we use the space charge limited current (SCLC) model, modified to account for the probe-sample geometry,[34,43] to spatially map hole mobility. Unlike current maps, mobility maps provide a

measure of charge carrier speed in the presence of an electric field, independent of local film thickness variations, making it more suitable for comparing different molecular systems.

Figure 4a and 4b show hole mobility maps for a *p*-DTS(FBTTh$_2$)$_2$:PC$_{71}$BM BHJ film (φ_{DTS} = 0.6, 0 vol. % DIO) and a single component *p*-DTS(FBTTh$_2$)$_2$ (0 vol. % DIO) film, respectively. In the *p*-DTS(FBTTh$_2$)$_2$:PC$_{71}$BM film, isolated high mobility hotspots can be observed. The single component *p*-DTS(FBTTh$_2$)$_2$ film presents high mobility hotspots bridged by moderate hole mobility regions. The corresponding hole mobility histograms exhibit right-skewed distributions (see Figure 4c), with long tails reaching towards higher hole mobilities. The long tails reflect the disparity in mobility between high mobility hotspots and surrounding areas that are poorly electrically connected with the hotspots.

Figure 4d and 4e present hole mobility maps for P3HT:PC$_{61}$BM BHJ and single component P3HT films, respectively. In contrast with the corresponding small molecule films, the hole mobility drops off more gradually near the high mobility hotspots, leading to a more spatially uniform hole mobility in the polymer films (line profiles are shown in the Supporting Information, Figure S3). This finding is reflected in the hole mobility histograms (Figure 4f) that are symmetrical and narrowly distributed compared to the histograms for the small molecule films. The greater uniformity of the hole mobility across the polymer films supports the observation that the polymer system exhibits more lateral current spreading, and hence possesses a greater degree of in-plane electrical connectivity, than the studied small molecule system.

Finally, when comparing the average hole mobility for the small molecule and polymer systems, shown in Table 1, we see that the mobility drop between the single component film and BHJ is more drastic for the small molecule. Namely, for the small molecule films, the hole mobility drops by 52 %, while for the polymer films, it drops by only 21 %. This result provides evidence that the greater lateral electrical connectivity in the polymer BHJ helps to maintain three-dimensional percolation for out-of-plane charge flow. In other words, despite there being less hole transport material in the BHJ when compared with the single component film, lateral pathways in the polymer BHJ help preserve a continuous hole transport network for out-of-plane percolation.

3. Conclusion

To elucidate the role played by lateral pathways during out-of-plane charge transport in organic BHJ thin films, we have introduced a C-AFM approach to quantify lateral current spreading in a vertical device geometry. Lateral hole current spreading in *p*-DTS(FBTTh$_2$)$_2$:PC$_{71}$BM BHJs correlated with the in-plane π-π stacking population of the donor, which scaled with the degree of donor-acceptor phase separation and the donor fraction. Greater lateral current spreading and higher spatial uniformity in hole mobility maps were observed in BHJs with a polymer donor, P3HT, despite a low in-plane π–π population, indicating increased lateral electrical connectivity within the polymer films due to transport along the polymer backbone. These results suggest the importance of lateral transport channels for promoting efficient and uniform out-of-plane charge flow in BHJs. It should be noted, however, that increased lateral current spreading will not necessarily translate to an overall improvement in out-of-plane charge flow, since efficient three-dimensional charge percolation also

depends on the presence of efficient vertical charge transport channels. This work provides a tool to disentangle the contribution of lateral pathways during three-dimensional charge percolation.

The developed methodology for probing lateral current spreading in a vertical device geometry is promising for unraveling the morphological requirements to promote three-dimensional electrical connectivity in BHJs for high-performance OSC operation. For example, the approach opens potential study of the effects of polymer backbone structure and molecular weight on current spreading. With the use of low work function electrodes,[51] it should also be possible to extend the approach to monitor electron current spreading in BHJs containing fullerene or non-fullerene acceptors. The devised method is potentially applicable to a wide range of electronic materials, for insight into charge transport anisotropy.

4. Methods

Sample Preparation: ITO coated glass substrates purchased from Colorado Concept Coating LLC were cleaned with DI water, acetone, and 2-propanol for 10 min each in an ultrasonic bath. Substrates were then dried under nitrogen flow and further cleaned by UV-ozone treatment for 20 min. PEDOT:PSS solution (Clevios PH 1000 from Heraeus) was spin coated onto the clean ITO-coated glass at 3000 rpm for 60 s to achieve a film thickness of 30 nm. Substrates were then dried on a hotplate at 150 °C for 20 min. The PEDOT:PSS-coated substrates were transferred into a nitrogen filled glovebox for active layer deposition.

All donor and acceptor molecules (*p*-DTS(FBTTh$_2$)$_2$, P3HT, PC$_{61}$BM, and PC$_{71}$BM) were purchased from Solaris Chem. Solutions of *p*-DTS(FBTTh$_2$)$_2$ and *p*-DTS(FBTTh$_2$)$_2$:PC$_{71}$BM were prepared in chlorobenzene from Sigma Aldrich (anhydrous, >99.8% purity) with a total concentration of 21 mg/ml. The donor:acceptor weight ratio and DIO (Sigma Aldrich) vol. % employed for solution preparation are specified in the results section. The solutions were stirred overnight at 70 °C and then stirred at 90 °C for 15 min prior to spin coating the warm solutions onto room temperature substrates at 1300 rpm for 60 s. The samples were then annealed at 75 °C for 15 min. The thickness of the resulting films was measured by atomic force microscopy (AFM) to be 82 nm with a standard deviation of 4 nm.

Solutions of P3HT and P3HT:PC$_{61}$BM were prepared in chlorobenzene from Sigma Aldrich (anhydrous, >99.8% purity) with a total concentration of 20 mg/ml. For the P3HT:PC$_{61}$BM blend, the donor:acceptor ratio was kept at 3:2. Solutions were stirred overnight at 90 °C prior to spin coating the room temperature solution at 1000 rpm for 60 s to achieve a film thickness of 80 nm and a standard deviation of 3 nm, measured by AFM. The samples were then annealed at 150°C for 15 min. Solutions for thin (25 nm) P3HT films were prepared in chloroform from Sigma Aldrich (anhydrous, > 99% purity) with a total concentration of 2 mg/ml. Solutions were stirred at 45 °C overnight before spin coating the room temperature solution at 400 rpm for 10 s, followed by 1000 rpm for 60 s. These samples were annealed at 220 °C for 45 minutes to promote the edge-on crystallization of P3HT.[52]

Microelectrode arrays were patterned by using TEM grids with 1.2 µm diameter holes (Quantifoil, 300M, Ted Pella, Inc.) as shadow masks. Au (50 nm) was thermally evaporated at a rate of 0.2 Å/s. The microelectrode area for each sample was determined from C-AFM current maps, due to a dependence of the electrode shape and area on the evaporation geometry (see C-AFM map shown in the Supporting Information, Figure S2). The measured microelectrode areas were between 2.1µm^2 to 3.8 µm^2.

Sample Characterization: An AIST Combiscope 1000 AFM was used for C-AFM current and hole mobility mapping in a nitrogen environment. BudgetSensors ElectriCont-G Au-coated cantilevers with a nominal spring constant of 0.2 N/m and a probe radius of less than 25 nm were used with an applied force of 7 nN and a bias voltage of -3 V applied to the substrate for C-AFM current mapping. Hole mobility mapping was performed by recording current-voltage curves at 11025 positions for each sample using BudgetSensors ElectriCont-G Pt-coated cantilevers with a nominal spring constant of 0.2 N/m. The hole mobility was extracted by using in-house developed MATLAB code to perform space-charge limited current (SCLC) analysis with modifications to account for the probe-sample geometry.[43] To identify the voltage range that best fit the SCLC regime, the code plotted log J versus log (V-V_{bi}) for each IV curve, where V_{bi} is the built-in voltage, and then selected the voltage range that results in a slope closest to 2. The hole mobility was extracted from the slope of $\sqrt{J}$ versus V within the selected voltage range.

GIWAXS measurements were performed at the 11-BM beamline of the National Synchrotron Light Source II (NSLS-II) at Brookhaven National Laboratory. For all samples, an X-ray wavelength of

0.09184 nm was employed with an incidence angle of about 0.1°, a sample-detector distance of 257 mm, and an exposure time of 10 s. In-plane and out-of-plane scattering profiles were obtained by using Fit2d GIWAXS software[53] to integrate over a sector with an angular width of 20°. Peak profiles were fit with single pseudo-Voigt functions and crystallite populations were determined by integrating the area under the peaks. As the in-plane *p*-DTS(FBTTh$_2$)$_2$ π–π stacking peak widths approached the resolution limit of the apparatus,[54] the average grain size was not quantified.

Supporting Information

Supporting Information is available from the Wiley Online Library or from the author.

Acknowledgements

This work was supported by the National Science Foundation (CAREER award DMR-1555028) and Binghamton University's Smart Energy Transdisciplinary Area of Excellence. This research also used resources of the Complex Materials Scattering (CMS- 11-BM) beamline of the National Synchrotron Light Source II, a U.S. Department of Energy (DOE) Office of Science User Facility operated for the DOE Office of Science by Brookhaven National Laboratory under Contract No. DE-SC0012704. The authors thank Dr. Ruipeng Li for assistance with using CMS-11-BM facilities.

Conflict of Interest

The authors declare no conflict of interest.

Received: ((will be filled in by the editorial staff))
Revised: ((will be filled in by the editorial staff))
Published online: ((will be filled in by the editorial staff))

References

[1] Y. Huang, E. J. Kramer, A. J. Heeger, G. C. Bazan, *Chem. Rev.* **2014**, *114*, 7006.

[2] M.-E. Ragoussi, T. Torres, *Chem. Commun.* **2015**, *51*, 3957.

[3] J. Hou, O. Inganäs, R. H. Friend, F. Gao, *Nat. Mater.* **2018**, *17*, 119.

[4] Y. Li, G. Xu, C. Cui, Y. Li, *Adv. Energy Mater.* **2018**, *8*, 1701791.

[5] J. Wu, M. Gao, Y. Chai, P. Liu, B. Zhang, J. Liu, L. Ye, *Mater. Reports: Energy* **2021**, *1*, 100062.

[6] M. Nam, J. Kang, J. Shin, J. Na, Y. Park, J. Cho, B. Kim, H. H. Lee, R. Chang, D.-H. Ko, *Adv. Energy Mater.* **2019**, *9*, 1901856.

[7] Y. Cui, Y. Wang, J. Bergqvist, H. Yao, Y. Xu, B. Gao, C. Yang, S. Zhang, O. Inganäs, F. Gao, J. Hou, *Nat. Energy* **2019**, *4*, 768.

[8] H. K. H. Lee, J. Wu, J. Barbé, S. M. Jain, S. Wood, E. M. Speller, Z. Li, F. A. Castro, J. R. Durrant, W. C. Tsoi, *J. Mater. Chem. A* **2018**, *6*, 5618.

[9] M. Mainville, M. Leclerc, *ACS Energy Lett.* **2020**, 1186.

[10] Q. Liu, Y. Jiang, K. Jin, J. Qin, J. Xu, W. Li, J. Xiong, J. Liu, Z. Xiao, K. Sun, S. Yang, X. Zhang, L. Ding, *Sci. Bull.* **2020**, *65*, 272.

[11] Y. Lin, M. I. Nugraha, Y. Firdaus, A. D. Scaccabarozzi, F. Aniés, A.-H. Emwas, E. Yengel, X. Zheng, J. Liu, W. Wahyudi, E. Yarali, H. Faber, O. M. Bakr, L. Tsetseris, M. Heeney, T. D. Anthopoulos, *ACS Energy Lett.* **2020**, *5*, 3663.

[12] M. Zhang, L. Zhu, G. Zhou, T. Hao, C. Qiu, Z. Zhao, Q. Hu, B. W. Larson, H. Zhu, Z. Ma, Z. Tang, W. Feng, Y. Zhang, T. P. Russell, F. Liu, *Nat. Commun.* **2021**, *12*, 309.

[13] Y. Cui, Y. Xu, H. Yao, P. Bi, L. Hong, J. Zhang, Y. Zu, T. Zhang, J. Qin, J. Ren, Z. Chen, C. He, X. Hao, Z. Wei, J. Hou, *Adv. Mater.* **2021**, *33*, 2102420.

[14] F. Zhao, C. Wang, X. Zhan, *Adv. Energy Mater.* **2018**, *8*, 1703147.

[15] B. C. Thompson, J. M. J. Fréchet, *Angew. Chemie Int. Ed.* **2008**, *47*, 58.

[16] S. van Bavel, E. Sourty, G. de With, S. Veenstra, J. Loos, *J. Mater. Chem.* **2009**, *19*, 5388.

[17] J. D. Roehling, K. J. Batenburg, F. B. Swain, A. J. Moulé, I. Arslan, *Adv. Funct. Mater.* **2013**, *23*, 2115.

[18] O. Wodo, J. D. Roehling, A. J. Moulé, B. Ganapathysubramanian, *Energy Environ. Sci.* **2013**, *6*, 3060.

[19] K. Vakhshouri, D. R. Kozub, C. Wang, A. Salleo, E. D. Gomez, *Phys. Rev. Lett.* **2012**, *108*, 26601.

[20] J. S. Mehta, J. M. Mativetsky, *ACS Appl. Energy Mater.* **2018**, *1*, 5656.

[21] S. Badgujar, C. E. Song, S. Oh, W. S. Shin, S.-J. Moon, J.-C. Lee, I. H. Jung, S. K. Lee, *J. Mater. Chem. A* **2016**, *4*, 16335.

[22] L. Yang, S. Zhang, C. He, J. Zhang, H. Yao, Y. Yang, Y. Zhang, W. Zhao, J. Hou, *J. Am. Chem. Soc.* **2017**, *139*, 1958.

[23] V. Vohra, K. Kawashima, T. Kakara, T. Koganezawa, I. Osaka, K. Takimiya, H. Murata, *Nat. Photonics* **2015**, *9*, 403.

[24] X. Li, Y. Wang, Q. Zhu, X. Guo, W. Ma, X. Ou, M. Zhang, Y. Li, *J. Mater. Chem. A* **2019**, *7*, 3682.

[25] T. Kumari, S. M. Lee, S.-H. Kang, S. Chen, C. Yang, *Energy Environ. Sci.* **2017**, *10*, 258.

[26] J. A. Love, I. Nagao, Y. Huang, M. Kuik, V. Gupta, C. J. Takacs, J. E. Coughlin, L. Qi, T. S. van der Poll, E. J. Kramer, A. J. Heeger, T.-Q. Nguyen, G. C. Bazan, *J. Am. Chem. Soc.* **2014**, *136*, 3597.

[27] J. M. Mativetsky, H. Wang, S. S. Lee, L. Whittaker-Brooks, Y.-L. Loo, *Chem. Commun.* **2014**, *50*, 5319.

[28] J. Zhang, Y. Zhang, J. Fang, K. Lu, Z. Wang, W. Ma, Z. Wei, *J. Am. Chem. Soc.* **2015**, *137*, 8176.

[29] S. Li, W. Liu, C.-Z. Li, T.-K. Lau, X. Lu, M. Shi, H. Chen, *J. Mater. Chem. A* **2016**, *4*, 14983.

[30] K. Levon, A. Margolina, A. Z. Patashinsky, *Macromolecules* **1993**, *26*, 4061.

[31] S.-S. Cheng, P.-Y. Huang, M. Ramesh, H.-C. Chang, L.-M. Chen, C.-M. Yeh, C.-L. Fung, M.-C. Wu, C.-C. Liu, C. Kim, H.-C. Lin, M.-C. Chen, C.-W. Chu, *Adv. Funct. Mater.* **2014**, *24*, 2057.

[32] R. Li, J. W. Ward, D.-M. Smilgies, M. M. Payne, J. E. Anthony, O. D. Jurchescu, A. Amassian, *Adv. Mater.* **2012**, *24*, 5553.

[33] S. Fabiano, H. Wang, C. Piliego, C. Jaye, D. A. Fischer, Z. Chen, B. Pignataro, A. Facchetti, Y.-L. Loo, M. A. Loi, *Adv. Funct. Mater.* **2011**, *21*, 4479.

[34] O. G. Reid, K. Munechika, D. S. Ginger, *Nano Lett.* **2008**, *8*, 1602.

[35] H. Qiu, X. Dong, J. H. Shim, J. Cho, J. M. Mativetsky, *Appl. Phys. Lett.* **2018**, *112*, 263102.

[36] B. L. M. Hendriksen, F. Martin, Y. Qi, C. Mauldin, N. Vukmirovic, J. Ren, H. Wormeester, A. J. Katan, V. Altoe, S. Aloni, J. M. J. Fréchet, L.-W. Wang, M. Salmeron, *Nano Lett.* **2011**, *11*, 4107.

[37] O. G. Reid, H. Xin, S. A. Jenekhe, D. S. Ginger, *J. Appl. Phys.* **2010**, *108*, 84320.

[38] J. M. Mativetsky, J. Tarver, X. Yang, B. E. Koel, Y.-L. Loo, *Org. Electron.* **2014**, *15*, 631.

[39] A. K. K. Kyaw, D. H. Wang, C. Luo, Y. Cao, T.-Q. Nguyen, G. C. Bazan, A. J. Heeger, *Adv. Energy Mater.* **2014**, *4*, 1301469.

[40] L. A. Perez, K. W. Chou, J. A. Love, T. S. van der Poll, D.-M. Smilgies, T.-Q. Nguyen, E. J. Kramer, A. Amassian, G. C. Bazan, *Adv. Mater.* **2013**, *25*, 6380.

[41] A. K. K. Kyaw, D. H. Wang, D. Wynands, J. Zhang, T.-Q. Nguyen, G. C. Bazan, A. J. Heeger, *Nano Lett.* **2013**, *13*, 3796.

[42] J. S. Mehta, P. S. Fernando, J. L. Grazul, J. M. Mativetsky, *ACS Appl. Energy Mater.* **2019**, *2*, 5146.

[43] S. W. Button, J. M. Mativetsky, *Appl. Phys. Lett.* **2017**, *111*, 83302.

[44] S. Engmann, F. A. Bokel, A. A. Herzing, H. W. Ro, C. Girotto, B. Caputo, C. V Hoven, E. Schaible, A. Hexemer, D. M. DeLongchamp, L. J. Richter, *J. Mater. Chem. A* **2015**, *3*, 8764.

[45] J. A. Love, C. M. Proctor, J. Liu, C. J. Takacs, A. Sharenko, T. S. van der Poll, A. J. Heeger, G. C. Bazan, T.-Q. Nguyen, *Adv. Funct. Mater.* **2013**, *23*, 5019.

[46] J. R. Tumbleston, B. A. Collins, L. Yang, A. C. Stuart, E. Gann, W. Ma, W. You, H. Ade, *Nat. Photonics* **2014**, *8*, 385.

[47] B. P. Rand, D. Cheyns, K. Vasseur, N. C. Giebink, S. Mothy, Y. Yi, V. Coropceanu, D. Beljonne, J. Cornil, J.-L. Brédas, J. Genoe, *Adv. Funct. Mater.* **2012**, *22*, 2987.

[48] N. Herath, S. Das, J. K. Keum, J. Zhu, R. Kumar, I. N. Ivanov, B. G. Sumpter, J. F. Browning, K. Xiao, G. Gu, P. Joshi, S. Smith, V. Lauter, *Sci. Rep.* **2015**, *5*, 13407.

[49] B. O'Connor, R. J. Kline, B. R. Conrad, L. J. Richter, D. Gundlach, M. F. Toney, D. M.

DeLongchamp, *Adv. Funct. Mater.* **2011**, *21*, 3697.

[50] F. C. Grozema, P. T. van Duijnen, Y. A. Berlin, M. A. Ratner, L. D. A. Siebbeles, *J. Phys. Chem. B* **2002**, *106*, 7791.

[51] Y. Kondo, M. Osaka, H. Benten, H. Ohkita, S. Ito, *ACS Macro Lett.* **2015**, *4*, 879.

[52] E. Verploegen, R. Mondal, C. J. Bettinger, S. Sok, M. F. Toney, Z. Bao, *Adv. Funct. Mater.* **2010**, *20*, 3519.

[53] A. P. Hammersley, S. O. Svensson, M. Hanfland, A. N. Fitch, D. Hausermann, *High Press. Res.* **1996**, *14*, 235.

[54] D.-M. Smilgies, *J. Appl. Crystallogr.* **2009**, *42*, 1030.

A conductive atomic force microscope-based procedure is introduced to monitor the contribution of lateral pathways during out-of-plane charge transport in bulk heterojunctions, similar to those used in organic solar cells. The experiments show that lateral electrical connectivity can promote spatially uniform charge collection and is linked with the presence of in-plane molecular π-π stacking and charge transport along a polymer backbone.

P.S. Fernando, J.S. Mehta, D.-M. Smilgies, and J.M. Mativetsky**

Probing the contribution of lateral pathways to out-of-plane charge transport in organic bulk heterojunctions